

A Fusion Approach for Water Area Classification Using Visible, Near Infrared and Synthetic Aperture Radar for South Asian Conditions

Shahryar K. Ahmad¹, Faisal Hossain², Hisham Eldardiry, and Tamlin M. Pavelsky

Abstract—Consistent estimation of water surface area from remote sensing remains challenging in regions such as South Asia with vegetation, mountainous topography, and persistent monsoonal cloud cover. High-resolution optical imagery, which is often used for global inundation mapping, is highly impacted by clouds, while synthetic aperture radar (SAR) imagery is not impacted by clouds and is affected by both topographic layover and vegetation. Here, we compare and contrast inundation extent measurements from visible (Landsat-8 and Sentinel-2) and SAR (Sentinel-1) imagery. Each data type (wavelength) has complementary strengths and weaknesses which were gauged separately over selected water bodies in Bangladesh. High-resolution cloud-free PlanetScope imagery at 3-m resolution was used as a reference to check the accuracy of each technique and data type. Next, the optical and radar images were fused for a rule-based water area classification algorithm to derive the optimal decision for the water mask. Results indicate that the fusion approach can improve the overall accuracy by up to 3.8%, 18.2%, and 8.3% during the wet season over using the individual products of Landsat8, Sentinel-1, and Sentinel-2, respectively, at three sites, while providing increased observational frequency. The fusion-derived products resulted in overall accuracy ranging from 85.8% to 98.7% and Kappa coefficient varying from 0.61 to 0.83. The proposed SAR-visible fusion technique has potential for improving satellite-based surface water monitoring and storage changes, especially for smaller water bodies in humid tropical climate of South Asia.

Index Terms—Area classification, remote sensing, synthetic aperture radar (SAR), visible imagery, water bodies.

I. INTRODUCTION

WETLANDS and small surface water bodies play an important role in groundwater recharge, flood control, ecosystem services, wildlife habitat, and even rural livelihood [1], [2]. Knowledge of the areal extent or size of water bodies is crucial to the understanding of access and

availability of water in the natural environment. However, manual identification and tracking of these numerous water bodies in a feasible and cost-effective way is challenging due to their dynamic inundation extent and depth controlled by the local hydrology of the region [3].

To address the challenges of manual identification, satellite remote sensing can be a valuable tool for automated extraction of water surface area. Satellites are particularly effective where *in situ* measurement networks for water surface elevation (which can be used to derive surface area in concert with a digital elevation model) are limited. In the past two decades, the use of optical and synthetic aperture radar (SAR) satellite remote sensing data has expanded for mapping and monitoring wetlands [1]. The usage of satellite imagery at optical wavelengths for water body delineation has been primarily derived from band ratios and indices that use the differences in spectral signature of water and surrounding features [18], [35]. The Landsat satellite products have, therefore, been extensively explored for monitoring lake dynamics [13]–[15], [19], [36], [37]. A detailed review of the literature on monitoring of surface water using optical sensors is presented in [8]. Although optical data have proven itself for areal classification of water bodies [3], the presence of vegetation and cloud cover in the scene can seriously limit scientific applications [8]. While the former obscures the inundation underneath the vegetation, blocking and shadow effects by clouds can reduce the image information and seriously impact the mapped water extent.

SAR data, on the other hand, collected by active sensors at longer wavelengths, are able to penetrate the clouds and vegetation to varying degrees, working both diurnally and nocturnally. Water, which has a high dielectric constant and is a specular reflector at the wavelengths of most SAR sensors, often produces very low backscatter, which aids in extracting the water bodies from sensed radar data [16]. Shen *et al.* [20] reviewed the existing literature for principles and methods in the SAR-based inundation mapping. Despite the advantages of active SAR data in mapping water extent, the side-looking geometry and the requirement of specular reflection may lead to misclassification of some water surface areas as radar shadow due to waves, uneven surface, vegetation (commission error), and layover or topography (omission error) [3], [16]. Extracting inundation extent using only one type of data (visible or SAR), therefore, provides limited value when the region has persistent clouds or mountainous topography and

Manuscript received May 28, 2019; revised September 22, 2019; accepted October 28, 2019. Date of publication November 19, 2019; date of current version March 25, 2020. This work was supported by the NASA Citizen Science for Earth Systems Program through the Project “Tracking Freshwater Storage in Lakes: Citizens and Satellites Implementation Phase” under Grant 80NSSC18M0099. (Corresponding author: Faisal Hossain.)

S. K. Ahmad, F. Hossain, and H. Eldardiry are with the Department of Civil and Environmental Engineering, University of Washington, Seattle, WA 98195 USA (e-mail: skahmad@uw.edu; fhossain@uw.edu; dardiry@uw.edu).

T. M. Pavelsky is with the Geological Sciences Department, University of North Carolina, Chapel Hill, NC 27599-3315 USA (e-mail: pavelsky@unc.edu).

Color versions of one or more of the figures in this article are available online at <http://ieeexplore.ieee.org>.

Digital Object Identifier 10.1109/TGRS.2019.2950705

vegetation around the water body. Such conditions are notably pronounced in tropical humid climates of South Asia, such as Bangladesh.

Mapping surface water bodies in South Asian environment presents a unique challenge. The tropical monsoon climate with strong seasonal cycle leads to a highly dynamic response of lakes and wetlands. The lake inundation expands swiftly over the peak flow season from May to October and then dries up as the monsoon recedes. The surface of the lakes usually hosts an abundance of dense vegetation, often in the form of thick free-floating plants that obstruct the inundation beneath from being accurately mapped. Given the high number of such small-scale bodies present in the region [see Fig. 1(d)], their monitoring is both challenging and important for the effective management of water and ecosystems.

In an effort to develop a more robust water extraction technique that is tailored to overcome challenges in humid tropical climates of South Asia, we aim to fuse complementary strengths of remote sensing data types. Various studies have targeted fusion of multiple sensor products for various goals, such as shoreline extraction [4], change detection [5], retrieving daily normalized difference vegetation index (NDVI) and leaf area index (LAI) [6], and temporal aggregation for land cover mapping [7]. Studies by Kaplan and Avdan [1], Huang *et al.* [8], and Irwin *et al.* [12] have monitored wetlands and surface water by different fusion techniques. Huang *et al.* [21] presented an automated classification of SAR data trained using prior surface water masks derived from Shuttle Radar Topography Mission (SRTM) water body data set (SWBD), and Landsat 8 derived composited dynamic surface water extent (DSWE) class probabilities and tested it on North American sites representing inland and coastal wet landscape. Slinski *et al.* [27] used passive Landsat and active SAR data in a clustering analysis to generate water masks in the drier climates of Ethiopia. Despite a large body of the literature on the fusion of remote sensing products, no study, to the best of author knowledge, has explored water bodies or wetlands of South Asia impacted by both monsoonal cloud cover and dense vegetation and has smaller extents. This article assesses a fusion technique to address water area classification in regions, where cloud cover and vegetation are major challenges in remote sensing-based monitoring of water bodies. Unlike other published methods, the computational and data storage constraints were addressed in our approach by using the cloud-based computing platform of Google Earth Engine (GEE) [9] and a computationally efficient rule-based classification approach.

II. STUDY AREAS AND DATA SOURCES

A. Test Sites

The accuracy and robustness of the proposed approach were tested on three lakes/wetlands (also locally termed “Haors”) with varying water extents located in northeastern Bangladesh (Fig. 1). Haors are seasonal water bodies with dual-land use during the course of a year [28]. From the months of May to October, the low-elevation land is inundated with transboundary runoff generated by the monsoon rains from mountains in neighboring India. These water bodies become a productive

fisheries ecosystem during the monsoon season [28]. As the waters recede in the postmonsoon season spanning November to April, the soil becomes rich in nutrients and organic matter. The Haor land becomes primed for rice cultivation from groundwater that is recharged by the preceding monsoon rains. The rice cultivation during this season (known as Boro rice) is existential to food security of Bangladesh [29], [30]. Hence, accurate and automated mapping of the spatial extent of Haors in the context of changing land use can inform policy decisions for managing postmonsoon water availability, premonsoon flash floods, and rice cultivation.

The “true” boundaries of all the test water bodies, encompassing the wet season extent, were digitized manually from reference data that are described in Section II-B. The maximum extents used for the water extraction analysis were 65.6, 7, and 1.3 km² for Korchar, Dekhar, and Ashulia Haors. The locations and digitized water boundaries of each site are shown in Fig. 1(a)–(c).

B. Tools and Data Used

We used three satellite remote sensing products with different spatial, temporal, and spectral characteristics. These include: 1) Landsat 8 Operational Land Imager (OLI) Tier 1 surface reflectance and top of atmosphere (TOA) reflectance, with 30-m spatial resolution and 8–16-day revisit period (hereafter “L8”); 2) Sentinel-1A C-band synthetic aperture radar ground-range detected (SAR GRD) with a spatial resolution of 10 m and 6-day revisit period (labeled as “S1”); and 3) Sentinel-2 multispectral instrument (MSI, Level-1C) with a spatial resolution of 10 m (for red, green, blue (RGB) and near-infrared (NIR) bands) and revisit period of five days (labeled as “S2”). These visible, NIR, and SAR sensors were chosen due to the public availability of their data and their complementary strengths in water detection. The three satellite products were retrieved for a three-year time period spanning 2016 to 2018. The number of scenes used for each product over this period of analysis is summarized in Table I, where multiple scenes were used within a day for some sites to cover the entire water boundaries (see Fig. 1) to be classified.

Each of the products has at least one strength that the fusion technique relies upon, namely, the difference in spectral signatures of water and its surroundings in the optical wavelengths and the ability of radar to penetrate cloud and certain vegetation coverage. The JavaScript API of GEE platform [9] was used for the processing of these remote sensing products, all of which are available in the GEE data catalog. GEE provides access to satellite data sets on a planetary scale and provides extensive computing power for image processing and analysis without the need for high-end processing capability locally. Details on the preprocessing and water extraction algorithm applied to each product are presented in Section III.

C. Reference Data

For the accuracy assessment of the delineated water extent, we used higher resolution imagery in the visible and NIR bands. Planet (formally known as Planet Labs) [10], with a constellation of more than 170 active CubeSats, has realized

TABLE I

NUMBER OF SCENES USED FOR EACH PRODUCT OVER 2016–2018.
MULTIPLE SCENES WERE USED PER DAY TO COVER THE STUDY AREA

Test Site	Number of Scenes		
	L8	S1	S2
Korchar Haor	104	271	128
Dekhhar Haor	79	229	128
Ashulia Haor	107	141	258

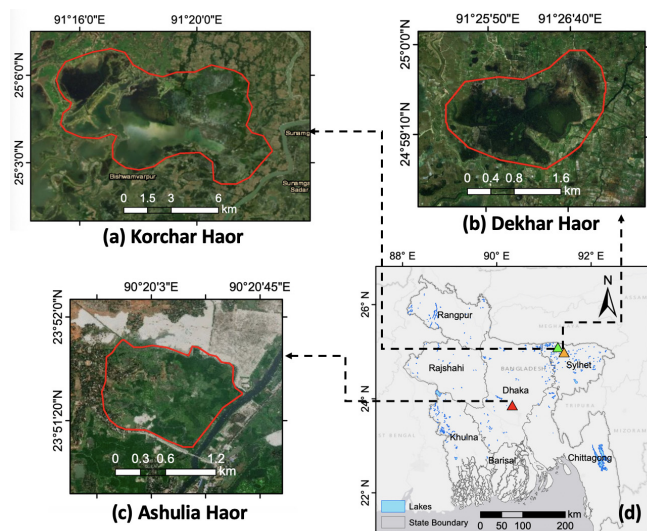


Fig. 1. (a)–(c) Locations and digitized boundaries for the three surface water bodies used in this study. (d) Surface water bodies (lakes and wetlands) over Bangladesh shown in blue.

daily global imaging in the visible and NIR at 3-m resolution. Recent studies have demonstrated the capabilities and usefulness of Planet data in easily extracting the water extent, such as those by Cooley *et al.* [22], [23]. Thus, the Level 3A PlanetScope Ortho Tile Product from Planet Labs with the orthorectified pixel size of 3.125 m and daily revisit time at nadir was acquired using the Planet Explorer imagery exploration tool [17] to obtain the reference water map, as explained later in Section III.

III. METHODOLOGY

An overview of the water area classification approach used in this study is shown in Fig. 2. The methodology begins first with processing the visible, NIR, and SAR reflectance data over the selected sites using two different water extraction algorithms as described in Sections III-A–III-C. The satellite data were acquired for the dates closest to the date of interest (DoI). The DoI is the user-defined day for which the water extent needs to be obtained. The output water extents from each satellite product were later fused together based on rules specific to each image type to derive the fused water extent. Accuracy assessment of fused water extent was then performed using high-resolution images.

A. Landsat-8-Based Water Extraction

The DSWE offered by U.S. Geological Survey (USGS) [11] for the L8 OLI product was incorporated here for water extraction. The algorithm was coded in the GEE platform

using JavaScript API to produce the DSWE output over any custom region of interest. The specifics of the algorithm are briefly described next. For details on DSWE algorithm, the reader is referred to [11].

The purpose of the DSWE algorithm is to account for vegetation over surface water bodies in the delineation procedure. It involves multiple levels of processing using geophysical information including a digital elevation model, slope, and hillshade, as well as quality flags encoding data on cloud, cloud shadow, and snow within each L8 scene. These are calculated based on the function of mask (FMask) algorithm [26]. The model used to generate DSWE is composed of five decision-rule-based diagnostic tests applied uniformly to all the pixels without requiring scene-based training. Three of the diagnostic tests are designed to detect if the pixel under consideration is fully covered by water (open water tests), while the other two tests detect inundation in the presence of vegetation or other nonwater land covers at the subpixel scale (partial water tests). Using the RGB, NIR, and shortwave IR bands 1 and 2 (SWIR1/2) from L8 surface reflectance product, the following indices are calculated: 1) modified normalized difference wetness index (MNDWI) = $(\text{green} - \text{SWIR1}) / (\text{green} + \text{SWIR1})$; 2) multiband spectral relationship visible (MBSRV) = $\text{green} + \text{red}$; 3) multiband spectral relationship near-infrared (MBSRN) = $\text{NIR} + \text{SWIR1}$; 4) automated water extent shadow (AWESH) = $\text{blue} + (2.5 \times \text{green}) - (1.5 \times \text{MBSRN}) - (0.25 \times \text{SWIR2})$; and 5) NDVI = $(\text{NIR} - \text{red}) / (\text{NIR} + \text{red})$. The open and partial water diagnostic tests are then performed for each pixel based on multiple thresholds applied to the spectral bands and the five calculated indices to produce a preliminary DSWE output. This study used default values for each threshold as specified in [11].

The next step is to refine the DSWE output by filtering out low-confidence water pixels using geophysical parameters including topography, slope, and hillshade for each pixel. Percent slope is used to remove the locations where the terrain is too steep to hold water. Similarly, any location where the terrain is too shaded is also filtered out. Next, the quality assessment (QA) bands obtained from the L8 TOA reflectance product are used to mask the cloud, cloud shadow, and snow, resulting in the final delineated DSWE output. The output band results into six possible values: 0 (not water), 1 (water—high confidence), 2 (water—moderate confidence), 3 (potential wetland/partial surface water conservative), 4 (low-confidence water/partial surface water aggressive), and 5 (masked out due to cloud, cloud shadow, or snow) [11]. Different confidence levels of inundation as well as the differentiation between no water and cloud/snow masked pixels were used later as one of the guiding factors in the fusion scheme described in Section III-D.

B. Sentinel-1-Based Water Extraction

The SAR imaging sensors of S1 send radar signals from the satellite toward the Earth at an off-nadir angle, and the backscatter off the Earth's surface is measured. The amount of backscatter is determined in part by the roughness of the surface, with smoother surfaces scattering less. Large flat surfaces like water scatter very little at C-, X-, and L-band

wavelengths most commonly used in SAR imaging, and they stand out as dark spots against relatively high-scattering land surface. This property is used to extract the surface water extent using a threshold on the backscatter value.

The S1 data were first preprocessed to filter the type of signal received by the sensor. The S1 GRD images in GEE catalog are detected, multilooped, processed to remove thermal noise, radiometrically calibrated, orthorectified, and geo-referenced SAR data. The co-polarized scenes with the vertical (VV) transmitter–receiver polarization (vertical transmitted and vertical received) were selected to ensure the images have same transmit/receive polarizations. One of the issues that exists with the radar product is the degradation of its quality with the signal dependent granular noise, also called “speckle.” The speckle is primarily caused by the phenomenon of interference of the returning wave at the transducer aperture. A focal median filter with $30\text{ m} \times 30\text{ m}$ window was applied to smoothen the image and, thus, reduce down the speckle noise. The incidence angle of the SAR images also plays an important role in the quality of the resulting classified product. At lower look angles, the surface spatial resolution in range decreases significantly (becomes coarser), while at higher angles, the signal-to-noise ratio is quite small for low-reflectivity targets such as wetlands [38]. Hence, the incidence angles (θ) were limited to the range $31.7^\circ < \theta < 45.4^\circ$. With the processed S1 image, a gray-level thresholding algorithm was applied for delineation. Considering the dynamic range of backscatter values for standing water of -24.3 to -12.6 dB as found by Liu [31], a threshold value of -13 dB was selected for classifying pixels less than the threshold as water.

C. Sentinel-2-Based Water Extraction

The third satellite product used for inundation area estimation is the multispectral S2 data set. The 10-m resolution (for RGB and NIR reflectance bands) adds value in terms of spatial granularity to the water extraction relative to the previously chosen 30-m L8 multispectral data set. The DSWE algorithm was also applied over the S2 bands to obtain the classified water map. However, as the algorithm in its current state and its thresholds are designed specifically for Landsat satellites, modifications are needed to apply the same thresholds for S2 due to differences in sensor characteristics and spectral bands [32]. Because the algorithm is yet to be modified by the official algorithm developer for a reliable application with S2, an approach that transforms the surface reflectance of S2 bands to that of L8 bands was incorporated so that the same thresholds for L8 can be used. The surface reflectance transformation functions for the approximately equivalent spectral bands of L8 and S2 were given by Zhang *et al.* [32] whose study region was located in southern Africa with different land cover classes, representative of a wide range of reflectance spectra and covering multiple seasons. The linear mapping functions from S2 to L8 for the bands used by the DSWE algorithm are tabulated in Table II. Furthermore, the QA60 bitmask band (at 60-m resolution) provided in S2 was used to obtain the cirrus and opaque cloud mask information.

TABLE II
TRANSFORMATION FUNCTIONS BETWEEN APPROXIMATELY EQUIVALENT BANDS OF L8 AND S2 FOR APPLYING L8-BASED DSWE THRESHOLDS TO S2 (AFTER ZHANG *et al.* [32])

Spectral band	Transformation function
Blue ($\sim 0.48\ \mu\text{m}$)	$L8 = 0.0003 + 0.9570 * S2$
Green ($\sim 0.56\ \mu\text{m}$)	$L8 = 0.0015 + 1.0304 * S2$
Red ($\sim 0.66\ \mu\text{m}$)	$L8 = 0.0041 + 0.9533 * S2$
Near Infrared, NIR ($\sim 0.66\ \mu\text{m}$)	$L8 = 0.0139 + 1.0157 * S2$
Shortwave Infrared, SWIR 1 ($\sim 1.61\ \mu\text{m}$)	$L8 = 0.0034 + 0.9522 * S2$
Shortwave Infrared, SWIR 2 ($\sim 2.21\ \mu\text{m}$)	$L8 = 0.0004 + 0.9711 * S2$

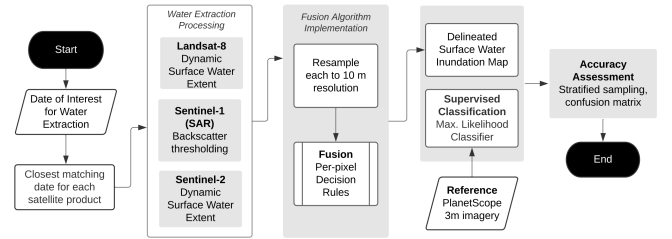


Fig. 2. Overview of the methodology for applying the fusion algorithm using three different satellite image products—L8, S1, and S2.

D. Proposed Fusion Approach

After each satellite image was independently processed to delineate the surface water extent, a fusion algorithm was created to take the advantage of the complementary strengths of the optical and radar data products. The fusion algorithm was applied on a per-pixel-basis, i.e., each pixel was evaluated for the optimal decision for water extraction. The algorithm (see Fig. 2) is described in detail below.

First, all three water extracted data sets were brought to the finest available resolution of 10 m to allow for a consistent comparison using GEE’s inbuilt reduceRegion function, with a scale argument set to 10 m across all data sets. Next, the dates of acquisition for each of the individual data sets were compared with the DoI for which the water extent was required. As the optical and radar images often cannot be acquired contemporaneously [8], any product falling outside the 30-day period from DoI was discarded from the fusion scheme. Although noteworthy changes to water extent can occur within the 30-day period, the period was selected based on the minimum gap for S1 of nearly 30 days between two consecutive acquisitions over the three-year period of analysis. A monthly timestep was also used by Slinski *et al.* [27] in obtaining the time series of surface water extent. Composite median of all the S1 images over the 30-day interval was obtained by calculating the focal median value at each pixel. Despite higher observational frequency, L8 and S2 exhibited larger gaps in available imagery due to high cloud cover, especially in monsoon seasons. This combination of imagery generates the following four scenarios: 1) all three data sets are available in the one-month interval; 2) only L8 and S1 available; 3) only S2 and S1 available; and 4) only S1 available. These cases require different fusion rules to be applied for the water extraction. The fourth scenario where only S1 is

TABLE III

FUSION ALGORITHM WITH DECISION RULES TO OBTAIN THE OPTIMAL WATER MASK FOR EACH PIXEL. THE THREE SCENARIOS ARE TABULATED IN (A)–(C), WHILE THE FOURTH (WITH ONLY S1 AVAILABLE) ASSUMES THE SAME OUTPUT AS S1. W: WATER; NW: NO WATER PRESENT; LNW: LOW CONFIDENCE OR NO WATER PRESENT (DSWE OUTPUT OF 0 OR 4); HLW: HIGH/MODERATE/LOW CONFIDENCE WATER (DSWE OUTPUT OF 1–4); HW: HIGH CONFIDENCE WATER (DSWE OUTPUT OF 1); HMW: HIGH/MODERATE CONFIDENCE WATER (DSWE OUTPUT OF 1–2); CLOUD: CLOUD COVERED PIXEL (DSWE OUTPUT OF 5); AND “–”: THE OUTPUT IS INDEPENDENT OF THE PIXEL’S STATE FOR THAT PRODUCT. (A) SCENARIO 1: ALL SATELLITE PRODUCTS (S1, L8, AND S2) AVAILABLE. (B) SCENARIO 2: ONLY S1 AND L8 AVAILABLE. (C) SCENARIO 3: ONLY S1 AND S2 AVAILABLE

(A)									
Product	Decision rule for the state of classified pixel								
	1	2	3	4	5	6	7	8	All Other
S1	W	W	–	–	–	W	W	W	
L8	HLW	–	HMW	HW		Cloud	–	LNW	
S2	–	HLW	HMW	–	HW	–	Cloud	LNW	
Decision	W	W	W	W	W	W	W	NW	NW
<i>Rationale</i>	High confidence	High confidence	High confidence	High confidence	High confidence	L8 Cloud	S2 Cloud	SAR Speckle	Low/No confidence

(B)						
Product	Decision rule for the state of classified pixel					
	1	2	3	4	5	All Other
S1	W	W	NW	NW	W	
L8	HLW	Cloud	HW	LNW, Cloud	NW	
Decision	W	W	W	NW	NW	NW
<i>Rationale</i>	High confidence	L8 Cloud	High confidence	Low confidence	SAR Speckle	Low/No confidence

(C) SCENARIO 3: ONLY S1 AND S2 AVAILABLE						
Product	Decision rule for the state of classified pixel					
	1	2	3	4	5	All Other
S1	W	W	NW	NW	W	
S2	HLW	Cloud	HW	LNW, Cloud	NW	
Decision	W	W	W	NW	NW	NW
<i>Rationale</i>	High confidence	S2 Cloud	High confidence	Low Confidence	SAR Speckle	Low/No confidence

available assumes the same output as the S1-based water extent. The decision rules implemented in the fusion scheme are summarized in Table III.

The rules presented in Table III were selected to compensate for the limitations of each product with the complementary strength of other products. For instance, the speckle noise in SAR (that persists even after applying the focal median filter) is reduced using the L8 and S2 results from the nearest day of acquisition. Similarly, on days when L8 or S2 experiences high cloud cover, the cloud-free S1 imagery was capitalized on in the fusion scheme to produce the most optimal estimate of the water mask over the selected water body. Different confidence levels from DSWE output were used to infer the cases of high confidence in classifying the output pixel state as water. For instance, when the L8 and S2 classify a pixel as water with either high or moderate confidence, there is a high confidence in the output pixel being water, irrespective of S1, and hence is classified as water [see decision rule 3 in Table III(a)]. Such a rule-based classification is computationally efficient and requires little or no training data for calibration.

E. Assessment of the Proposed Fusion Technique

To assess the accuracy of delineated water area using the individual satellite products and the fusion approach, 3-m resolution PlanetScope image was used to classify water extent. Due to the absence of *in situ* data, the classified PlanetScope

map was used as reference [22], [33], [34]. It needs to be mentioned here that the use of Planet imagery for assessment has weaknesses of its own such as the product’s optical nature which can lead to biases similar to other optical sensors used here regarding vegetation and cloud cover. To minimize some of these biases, care was taken while acquiring the PlanetScope scenes to ensure they were completely cloud-free and as closely matched in time as possible to the available L8, S1, and S2 scenes over each water body. Images for three different seasons (wet, dry, and intermediate) were downloaded and processed separately for the comparison. Supervised classification was performed on each of them using the maximum likelihood classification. The accuracy of fusion-based output was quantified in terms of the confusion matrix and user’s/producer’s accuracy values for specific days in different seasons. A time series of surface water extent was also derived from the individual water extraction procedures and the fusion approach to assess the temporal consistency. In addition, spatial maps were visually compared to evaluate spatial consistency.

IV. CASE STUDY RESULTS

A. Temporal Consistency: Time Series of Water Inundated Area

The areas derived from the extraction algorithms of L8, S2, S1, and the fusion technique over 2016–2018 are shown in Fig. 3 for the three selected sites. The cyclical pattern of water

TABLE IV
ACCURACY ASSESSMENT FOR THE THREE SITES OVER DIFFERENT SEASONS

Site	Approach	Water		Non-Water		Overall accuracy (%)	Kappa coefficient
		User Accuracy (%)	Producer Accuracy (%)	User Accuracy (%)	Producer Accuracy (%)		
Korchar Haor	Oct 2018 (wet)						
	L8	93.0	82.1	60.6	81.7	82.0	0.57
	S1	90.3	64.7	43.1	79.4	68.4	0.35
	S2	92.6	85.4	64.7	79.7	83.9	0.60
	FUSION	91.2	90.0	71.6	73.4	85.8	0.63
	Dec 2018 (intermediate)						
	L8	86.3	82.1	83.4	87.4	84.8	0.70
	S1	87.1	65.8	73.2	90.5	78.4	0.57
	S2	82.7	79.7	80.9	83.8	81.8	0.64
	FUSION	86.7	85.0	85.9	86.6	85.8	0.72
	Mar 2018 (dry)						
	L8	79.6	55.7	98.4	99.5	97.9	0.64
	S1	73.8	62.0	67.2	78.0	70.0	0.40
	S2	77.6	64.3	98.7	99.3	98.1	0.69
FUSION	84.0	58.6	98.6	98.8	98.2	0.69	
Dekhar Haor	Oct 2016 (wet)						
	L8 (cloud affected)	91.1	19.0	24.5	93.4	35.4	0.06
	S1	99.9	69.4	47.7	99.7	76.0	0.50
	S2	92.9	97.9	90.7	73.2	92.5	0.76
	FUSION	96.2	96.5	87.3	86.3	94.2	0.83
	Feb 2017 (dry)						
	L8	63.2	54.5	99.0	99.3	98.3	0.58
	S1	100	36.4	98.6	100	98.6	0.53
	S2	67.3	75.0	99.4	99.1	98.6	0.70
	FUSION	69.6	72.7	99.4	97.1	98.7	0.70
Ashulia Haor	May 2018 (wet)						
	L8	75.2	65.1	89.1	93.0	86.0	0.61
	S1	89.5	10.4	77.5	99.6	77.8	0.14
	S2	60.8	25.3	79.6	94.7	77.7	0.25
	FUSION	70.4	71.0	90.6	90.3	86.0	0.61
	Mar 2018 (dry)						
	L8	88.3	63.1	98.4	99.6	98.1	0.73
	S1	100	19.0	96.6	100	96.6	0.31
S2	84.1	88.1	99.4	99.2	98.7	0.85	
FUSION	86.1	81.0	99.2	99.4	98.7	0.83	

TABLE V
COMPARISON OF SURFACE WATER AREA DERIVED FROM THE THREE TECHNIQUES

Approach	Area (km ²)		
	Korchar (Oct 2018)	Dekhar (Oct 2016)	Ashulia (Sep 2018)
APWC	26.88	1.02	0.58
Fusion	52.70	3.09	0.84
PlanetScope	54.39	3.17	0.77

area due to monsoonal hydrology is clearly apparent at all the three sites.

It is apparent from Fig. 3 that L8 and S2 suffered from high-cloud cover issues especially during the wet seasons that leads to lower area estimates. In addition, while S1 tends to produce lower estimates of inundation extent, L8 and S2 result in similar results during cloud-free days. The fused technique is able to reproduce a temporally consistent estimate of water areas, filling up the gaps left by the optical images during high-cloud cover in monsoon-dominated months. Some of the sudden changes in fusion-derived time series persist due to the unavailability of one or both the optical data sets (due to high-cloud cover).

B. Spatial Consistency: Maps of Delineated Water Extent

The spatial consistency of the resulting inundation extent is first assessed by visually comparing the classified water maps produced by different sensors against that obtained from the reference PlanetScope imagery. The delineated water maps are shown for different seasons (wet, dry, and intermediate) for all the three sites in Fig. 4, along with the respective surface water area. It can be observed that the fusion-based water extent is spatially consistent with the PlanetScope's reference map. Also, the area values from PlanetScope and fusion-derived water mask are closest, as compared to those from individual products.

C. Accuracy Assessment

Accuracy was assessed for each remote sensing data type and technique against the reference data set. For estimation of the classification accuracy, 2000 points were selected using stratified random strategy. The points were randomly distributed within the two classes of water and no water, where each class has a number of points proportional to its relative area. Among four different sampling techniques, the stratified random sampling method resulted in the highest classification accuracy in a study by Ramezan *et al.* [24], and it was also

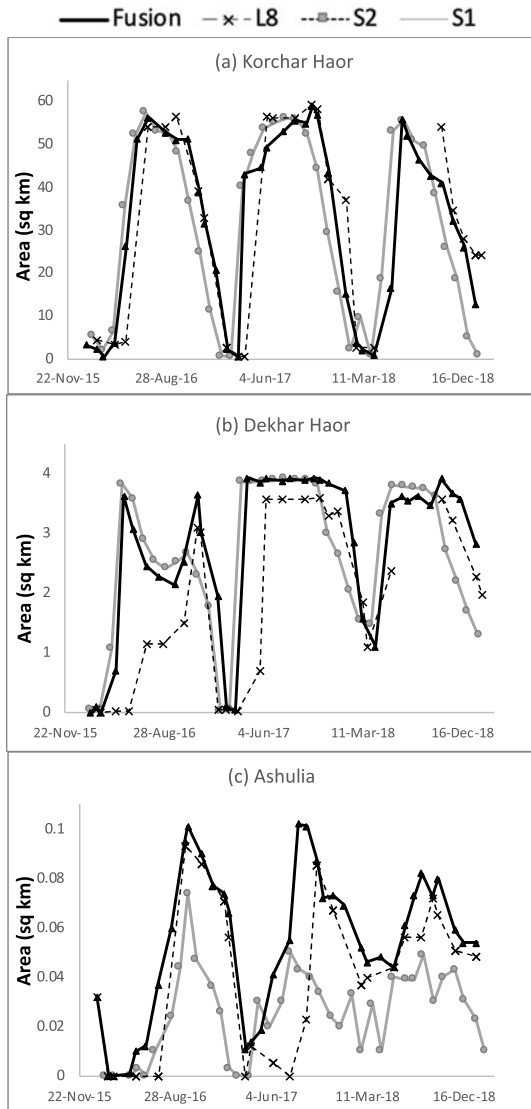


Fig. 3. Time series of extract water surface areas over 2016–2018 from L8, S1, S2, and fusion approach are compared for three selected sites. (a) Korchar Haor. (b) Dekhar Haor. (c) Ashulia.

used by Slinski *et al.* [27]. The confusion matrix and detailed accuracy assessment with user and producer accuracies are shown in Table IV for each of the three sites. The accuracy is reported for both the water and nonwater class detection. The overall accuracy and Kappa coefficient that accounts for the possibility of agreement occurring by chance are also obtained.

The highest overall accuracies were obtained during the dry seasons for all the three sites, with the overall accuracy between 85.8% and 98.7% and Kappa coefficients ranging from 0.61 to 0.83. During the wet season, the fusion approach resulted in improvements in overall accuracy of up to 3.8%, 18.2%, and 8.3% over using the individual products of L8, S1, and S2, respectively, across the three sites, while not considering the cloud-affected L8/S2 images. For the considered dry/intermediate seasons, the improvements reaching up to 1%, 28.2%, and 4% were obtained over L8, S1, and S2, respectively. The underestimation of water area using S1 is apparent, with lower producer and user accuracies for

the water and nonwater classes, respectively. The effect of S1 speckle can be seen for Korchar Haor during the dry season (March 2018) with very low user accuracy of the water and nonwater classes (pixel on classified map not corresponding to the same on ground). The highest accuracies were obtained during the dry seasons with the three products performing similar to the fusion output, except S1, which suffers from high speckle for Korchar Haor in the March 2018 water-classified map.

D. Comparison of the Fusion Approach With a Comparable Method

Comparison of results obtained from the fusion approach was made against a recently published and comparable algorithm recent literature. This method is called active–passive surface water classification (APWC) [27] and was implemented over the three Haors in GEE to obtain the water extent for comparison with the fusion-derived estimates. The APWC method was chosen specifically because it uses the combination of active (Sentinel-1 SAR) and passive (Landsat 7/8) sensors and is one of the first studies to generate accurate monthly water body maps at 10-m resolution, in this case in Ethiopia. However, the assessment of the technique for more humid, monsoonal environments such as those found in South Asia has not yet been performed. The APWC method uses K -means cluster analysis to obtain the water mask which can be implemented on the GEE platform.

This makes comparison more convenient with the fusion approach in this study coded in the same GEE environment. For performing the K -means cluster analysis, five clusters were used ($K = 5$) and the cluster corresponding to water was selected based on the PlanetScope-derived water map. The results for classified water extent from APWC for each site are shown in Fig. 5, while Table V shows the comparison of the respective areas with those derived from fusion approach and PlanetScope’s reference imagery.

As our comparison suggests, for small water bodies in Bangladesh for which APWC has not yet been tested, the method tends to underestimate the inundation extent while detecting more classes within the water mask. Furthermore, decreasing the number of clusters from five (not shown here) resulted in a greater number of false positives. This result suggests that our proposed fusion algorithm based on decision rules and synergistic use of active and passive remote sensing data is appropriately tailored for water body delineation in South Asian environments.

V. DISCUSSION AND CONCLUSION

This article proposes a fusion technique for water area classification tailored for the humid climate of South Asia, where persistent cloud cover, vegetation, and mountainous topography present challenges. The technique takes advantage of complementary strengths of different remote sensing data and produces the most optimal water mask possible with the available data and higher observational frequency. Remote sensing images from L8, S1, and S2 were processed independently to extract surface water extent over three different

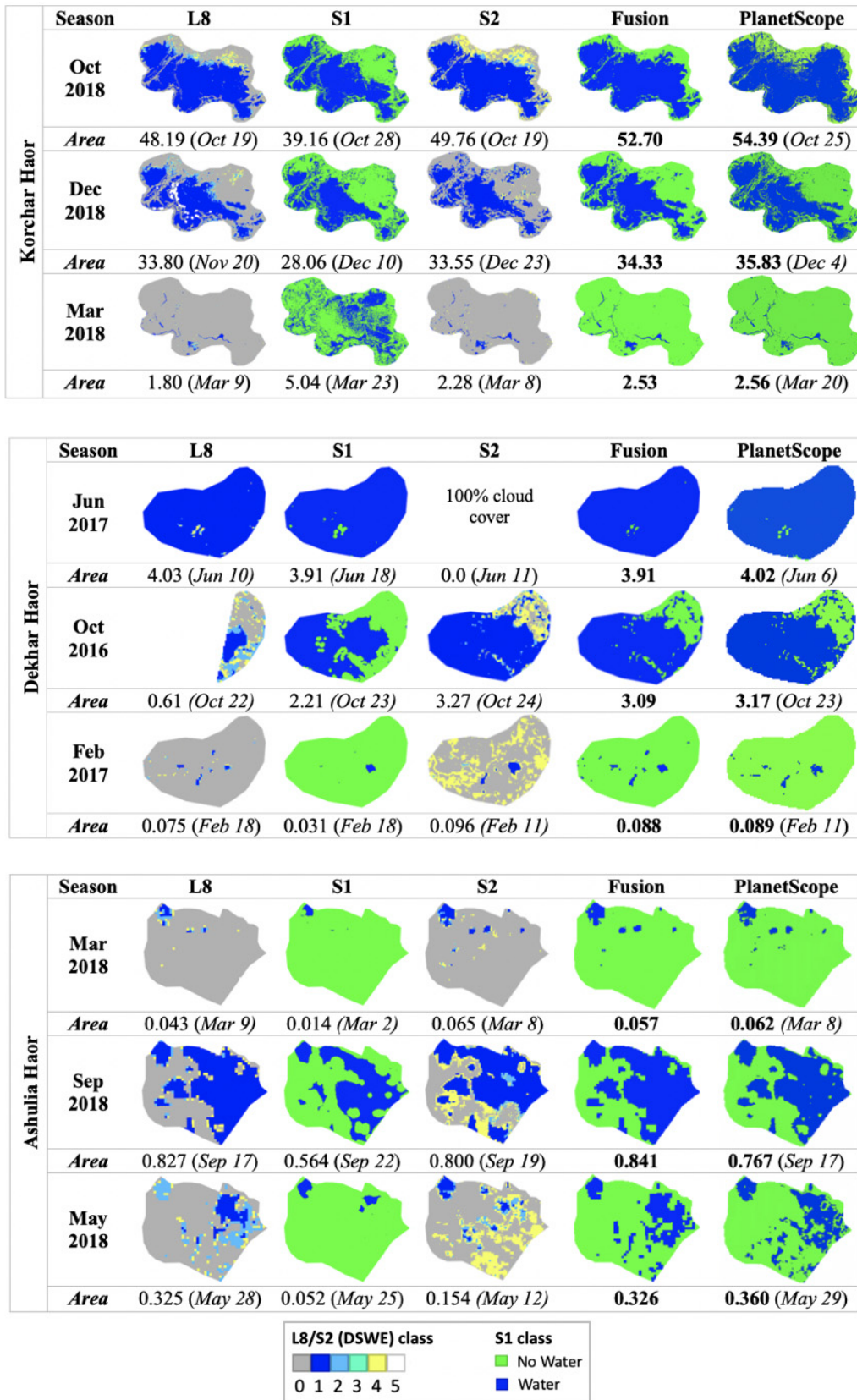


Fig. 4. Water inundation maps derived from the individual satellite products and the fusion approach for the three sites during representative months of wet, dry, and intermediate seasons, compared with the PlanetScope reference water inundation. The water areas and the corresponding dates of acquisition in brackets are specified below each map.

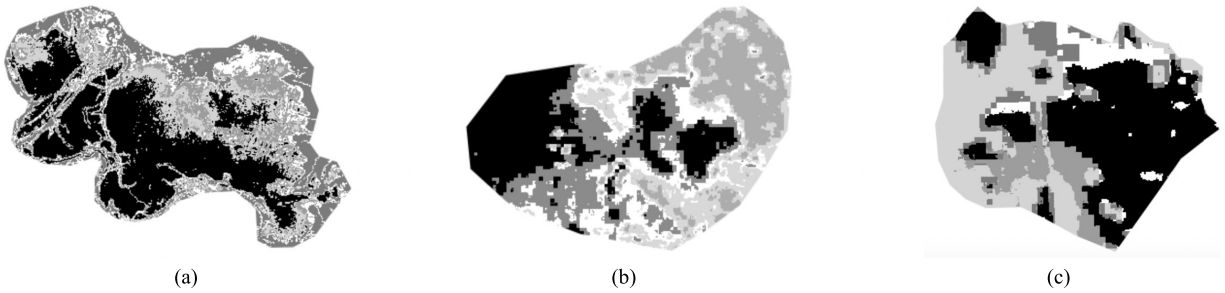


Fig. 5. APWC-derived water mask (black) using K -means clustering for the three Haors. Other colors denote the remaining four classes resulting from the APWC K -means cluster analysis ($K = 5$). (a) Korchar (October 2018). (b) Dekhar (October 2016). (c) Ashulia (September 2018).

surface water bodies (lakes) with different areas and seasonal dynamics. The GEE platform used here also allows for application and assessment of the technique over any other region of interest.

The fusion approach yielded temporally consistent time series over the three-year period of analysis. The output was able to fill the major gaps in L8 and S2 time series due to high cloud cover, especially during the monsoon seasons. Moreover, the fusion approach is able to address the limitation of underestimation in the radar-based S1 sensor. The speckle noise was also reduced using the spatially consistent results from L8 and S2 images. The disagreement and misclassification from the individual remote sensing techniques highlight the weaknesses of each technique and the advantage of using a fusion approach over small lakes in a tropical monsoon climate.

The fusion technique applied over the South Asian waters was compared with outputs from the already published APWC algorithm [27]. The latter, based on the K -means clustering, resulted in a greater number of missed water pixels and underestimation in surface water extent. The relatively better estimate from the proposed fusion approach is indicative of its ability to perform in challenging environments with shallower, smaller, and vegetation-dominated water bodies. While the clustering-based APWC successfully generates accurate water body maps in drier climate of Ethiopia in [27], it may need modification to be suitable for South Asian water bodies. To be fair to APWC, the proposed fusion technique benefits from the well-established DSWE algorithm for L8 and S2, while APWC does not. It should also be noted that the fusion approach is limited by the time difference in the acquisition dates between optical and radar images. The worst-case scenario with the difference of one month might cause discrepancies in the derived area, especially during the wetter seasons with high-cloud cover for optical images.

Overall, the proposed fusion scheme is able to produce spatially and temporally robust and more frequent estimate of water area when compared with those obtained from individual sensors. It is important that such a technique, using freely available remote sensing products, be used to improve automated space-based monitoring of water bodies and, hence, inform policy for better management of the Earth's freshwater resources. Future extension of this work should consider the use of polarimetric SAR data as an alternative approach to the SAR data used here [39].

In combination with water surface elevations obtained from *in situ* gauges, some of which we have installed in the Haors described here as part of a citizen science project, it may be possible to use the satellite-based measurements of inundation extent described here to estimate changes in water volume over time. This measurement, which is critical for understanding regional water balance variations, is also a focal point of the upcoming Surface Water and Ocean Topography (SWOT) satellite mission, scheduled for launch in 2021 [25]. Fusion of SWOT with other sensors, using methods stemming from this study, may result in improved understanding of water resources in monsoonal environments like South Asia.

REFERENCES

- [1] G. Kaplan and U. Avdan, "Sentinel-1 and Sentinel-2 data fusion for wetlands mapping: Balikdami, Turkey," in *Proc. Int. Arch. Photogramm. Remote Sens. Spatial Inf. Sci.*, 2018, pp. 729–734, doi: [10.5194/isprs-archives-XLII-3-729-2018](https://doi.org/10.5194/isprs-archives-XLII-3-729-2018).
- [2] A. Sarkar and S. K. Jain, "Using Remote Sensing data to study wetland dynamics—A case study of Harike Wetland," in *Proc. 12th World Lake Conf.*, 2007, pp. 680–684.
- [3] C. Prigent, E. Matthews, F. Aires, and W. B. Rossow, "Remote sensing of global wetland dynamics with multiple satellite data sets," *Geophys. Res. Lett.*, vol. 28, no. 24, pp. 4631–4634, 2001.
- [4] S. A. Manaf, N. Mustapha, M. N. Sulaiman, N. A. Husin, and M. R. A. Hamid, "Comparison of classification techniques on fused optical and SAR images for shoreline extraction: A case study at Northeast coast of Peninsular Malaysia," *J. Comput. Sci.*, vol. 12, no. 8, pp. 399–411, 2016.
- [5] D. Seo, Y. Kim, Y. Eo, M. Lee, and W. Park, "Fusion of SAR and multispectral images using random forest regression for change detection," *ISPRS Int. J. Geo-Inf.*, vol. 7, no. 10, p. 401, 2018, doi: [10.3390/ijgi7100401](https://doi.org/10.3390/ijgi7100401).
- [6] R. Houborg and M. McCabe, "Daily retrieval of NDVI and LAI at 3 m resolution via the fusion of CubeSat, Landsat, and MODIS data," *Remote Sens.*, vol. 10, no. 6, p. 890, 2018.
- [7] L. Carrasco, A. W. O'Neil, R. D. Morton, and C. S. Rowland, "Evaluating combinations of temporally aggregated Sentinel-1, Sentinel-2 and Landsat 8 For land cover mapping with Google Earth Engine," *Remote Sens.*, vol. 11, no. 3, p. 288, 2019.
- [8] C. Huang, Y. Chen, S. Zhang, and J. Wu, "Detecting, extracting, and monitoring surface water from space using optical sensors: A review," *Rev. Geophys.*, vol. 56, no. 2, pp. 333–360, 2018.
- [9] N. Gorelick, M. Hancher, M. Dixon, S. Ilyushchenko, D. Thau, and R. Moore, "Google Earth Engine: Planetary-scale geospatial analysis for everyone," *Remote Sens. Environ.*, vol. 202, pp. 18–27, Dec. 2017.
- [10] Planet Team. (2018). *Planet Application Program Interface: In Space for Life on Earth*. Planet Labs. [Online]. Available: <https://api.planet.com>
- [11] J. W. Jones, "Improved automated detection of subpixel-scale inundation—Revised dynamic surface water extent (DSWE) partial surface water tests," *Remote Sens.*, vol. 11, no. 4, p. 374, 2019.
- [12] K. Irwin, D. Beaulne, A. Braun, and G. Fotopoulos, "Fusion of SAR, optical imagery and airborne LiDAR for surface water detection," *Remote Sens.*, vol. 9, no. 9, p. 890, 2017.

- [13] J. Li and Y. Sheng, "An automated scheme for glacial lake dynamics mapping using Landsat imagery and digital elevation models: A case study in the Himalayas," *Int. J. Remote Sens.*, vol. 33, pp. 5194–5213, 2012.
- [14] Y. Li, X. Gong, Z. Guo, K. Xu, D. Hu, and H. Zhou, "An index and approach for water extraction using Landsat—OLI data," *Int. J. Remote Sens.*, vol. 37, no. 16, pp. 3611–3635, 2016.
- [15] K. Zhai, X. Wu, Y. Qin, and P. Du, "Comparison of surface water extraction performances of different classic water indices using OLI and TM imageries in different situations," *Geo-Spatial Inf. Sci.*, vol. 18, no. 1, pp. 32–42, 2015.
- [16] L. White, B. Brisco, M. Daboor, A. Schmitt, and A. Pratt, "A collection of SAR methodologies for monitoring wetlands," *Remote Sens.*, vol. 7, no. 6, pp. 7615–7645, Jun. 2015.
- [17] Planet Team. (2017). *Planet Imagery Product Specification*. Planet Labs. [Online]. Available: https://www.planet.com/products/satellite-imagery/files/Planet_Combined_Imagery_Product_Specs_December2017.pdf
- [18] H. Jiang, M. Feng, Y. Zhu, N. Lu, J. Huang, and T. Xiao, "An automated method for extracting rivers and lakes from Landsat imagery," *Remote Sens.*, vol. 6, no. 6, pp. 5067–5089, 2014.
- [19] J.-F. Pekel, A. Cottam, N. Gorelick, and A. S. Belward, "High-resolution mapping of global surface water and its long-term changes," *Nature*, vol. 540, no. 7633, pp. 418–422, 2016.
- [20] X. Shen, D. Wang, K. Mao, E. Anagnostou, and Y. Hong, "Inundation extent mapping by synthetic aperture radar: A review," *Remote Sens.*, vol. 11, no. 7, p. 879, 2019.
- [21] W. Huang *et al.*, "Automated extraction of surface water extent from Sentinel-1 data," *Remote Sens.*, vol. 10, no. 5, p. 797, 2018.
- [22] S. W. Cooley, L. C. Smith, L. Stepan, and J. Mascaro, "Tracking dynamic northern surface water changes with high-frequency planet cubesat imagery," *Remote Sens.*, vol. 9, no. 12, p. 1306, 2017.
- [23] S. W. Cooley, L. C. Smith, J. C. Ryan, L. H. Pitcher, and T. M. Pavelsky, "Arctic-boreal lake dynamics revealed using CubeSat imagery," *Geophys. Res. Lett.*, vol. 46, no. 4, pp. 2111–2120, 2019.
- [24] C. A. Ramezan, T. A. Warner, and A. E. Maxwell, "Evaluation of Sampling and Cross-Validation Tuning Strategies for Regional-Scale Machine Learning Classification," *Remote Sens.*, vol. 11, no. 2, p. 185, 2019.
- [25] S. Biancamaria, D. P. Lettenmaier, and T. M. Pavelsky, "The SWOT mission and its capabilities for land hydrology," in *Remote Sensing and Water Resources*. Cham, Switzerland: Springer, 2016, pp. 117–147.
- [26] Z. Zhu and C. E. Woodcock, "Object-based cloud and cloud shadow detection in Landsat imagery," *Remote Sens. Environ.*, vol. 118, pp. 83–94, Mar. 2012.
- [27] K. M. Slinski, T. S. Hogue, and J. E. McCray, "Active-passive surface water classification: A new method for high-resolution monitoring of surface water dynamics," *Geophys. Res. Lett.*, vol. 46, no. 9, pp. 4694–4704, 2019, doi: [10.1029/2019GL082562](https://doi.org/10.1029/2019GL082562).
- [28] M. Kamruzzaman and R. Shaw, "Flood and sustainable agriculture in the Haor basin of Bangladesh: A review paper," *Universal J. Agric. Res.*, vol. 6, no. 1, pp. 40–49, 2018.
- [29] S. G. Hussain, "Role of rice in food security of Bangladesh," in *Food Security: Quality Management, Issues and Economic Implications*, M.A. Jones, and F.E. Hernandez, Eds. Hauppauge, NY, USA: Nova Science Publishers, 2012, pp. 127–148, ch. 5.
- [30] Y. Chen and C. Lu, "A comparative analysis on food security in Bangladesh, India and Myanmar," *Sustainability*, vol. 10, no. 2, p. 405, 2018.
- [31] C. Liu, "Analysis of Sentinel-1 SAR data for mapping standing water in the Twente region," M.S. thesis, Univ. Twente, Enschede, The Netherlands, 2016.
- [32] H. K. Zhang *et al.*, "Characterization of Sentinel-2A and Landsat-8 top of atmosphere, surface, and nadir BRDF adjusted reflectance and NDVI differences," *Remote Sens. Environ.*, vol. 215, pp. 482–494, Sep. 2018.
- [33] M. Gašparović, D. Medak, I. Pilaš, L. Jurjević, and I. Balenović, "Fusion of Sentinel-2 and planetscope imagery for vegetation detection and monitoring," in *Proc. Int. Arch. Photogramm., Remote Sens. Spatial Inf.*, 2018, pp. 155–160.
- [34] M. F. McCabe, B. Aragon, R. Houborg, and J. Mascaro, "CubeSats in hydrology: Ultrahigh-resolution insights into vegetation dynamics and terrestrial evaporation," *Water Resour. Res.*, vol. 53, no. 7, pp. 10017–10024, 2017.
- [35] G. Q. Zhang, G. Zheng, Y. Gao, Y. Xiang, Y. Lei, and J. Li, "Automated water classification in the tibetan plateau using Chinese GF-1 WFV data," *Photogramm. Eng. Remote Sens.*, vol. 83, no. 7, pp. 509–519, 2017.
- [36] Z. Zou *et al.*, "Divergent trends of open-surface water body area in the contiguous United States from 1984 to 2016," *Proc. Nat. Acad. Sci. USA*, vol. 115, no. 15, pp. 3810–3815, Apr. 2018.
- [37] G. Zhang *et al.*, "Reilly, "Regional differences of lake evolution across China during 1960s–2015 and its natural and anthropogenic causes," *Remote Sens. Environ.*, vol. 221, pp. 386–404, Feb. 2019.
- [38] T. Nagler, H. Rott, E. Ripper, G. Bippus, and M. Hetzenecker, "Advancements for snowmelt monitoring by means of Sentinel-1 SAR," *Remote Sens.*, vol. 8, no. 4, p. 348, 2016.
- [39] E. Ferrentino, F. Nunziata, and M. Migliaccio, "Full-polarimetric SAR measurements for coastline extraction and coastal area classification," *Int. J. Remote Sens.*, vol. 38, no. 23, pp. 7405–7421, 2017.



Shahryar K. Ahmad received the B.Tech. degree in civil engineering from IIT Kanpur, Kanpur, India, in 2016, and the M.S. degree in civil and environmental engineering from the University of Washington, Seattle, WA, USA, in 2017, where he is currently pursuing the Ph.D. degree, with a focus on the field of remote sensing and numerical weather prediction applications for water-energy and food security issues.



Faisal Hossain received the B.S. degree from IIT Varanasi, Varanasi, India, in 1996, the M.S. degree from the National University of Singapore, Singapore, in 1999, and the Ph.D. degree from the University of Connecticut, Storrs, CT, USA, in 2004.

He is currently a Professor with the Department of Civil and Environmental Engineering, University of Washington, Seattle, WA, USA. His research interests include hydrologic remote sensing, sustainable water resources engineering, transboundary water resources management, and engineering education.



Hisham Eldardiry received the B.S. degree in civil engineering from the University of Alexandria, Alexandria, Egypt, in 2010, and the M.S. degree from the University of Louisiana at Lafayette, Lafayette, LA, USA, in 2014. He is currently pursuing the Ph.D. degree with the University of Washington, Seattle, WA, USA, with a focus on water–food and energy sustainability of the Nile river basin using remote sensing and physical models.



Tamlin M. Pavelsky received the B.A. degree from Middlebury College, Middlebury, VT, USA, in 2001, and the M.A. and Ph.D. degrees from the University of California at Los Angeles (UCLA), Los Angeles, CA, USA, in 2004 and 2008, respectively.

He is currently an Associate Professor with the Department of Geological Sciences, University of North Carolina, Chapel Hill, NC, USA. His research interests include global hydrology using remote sensing, field work, and modeling.